applied sciences

MDPI

Article

Aeroelastic Oscillations of Cantilever Beams Reinforced by Carbon Nanotubes Based on a Modified Third-Order Piston Theory

Mehdi Alimoradzadeh [1], Francesco Tornabene [2,*] and Rossana Dimitri [2]

[1] Department of Mechanical Engineering, Najafabad Branch, Islamic Azad University, Najafabad 8514143131, Iran; mehdi.alimoradzade@gmail.com
[2] Department of Innovation Engineering, University of Salento, 73100 Lecce, Italy; rossana.dimitri@unisalento.it
* Correspondence: francesco.tornabene@unisalento.it

Abstract

This work analyzes the aero-elastic oscillations of cantilever beams reinforced by carbon nanotubes (CNTs). Four different distributions of single-walled CNTs are assumed as the reinforcing phase, in the thickness direction of the polymeric matrix. A modified third-order piston theory is used as an accurate tool to model the supersonic air flow, rather than a first-order piston theory. The nonlinear dynamic equation governing the problem accounts for Von Kármán-type nonlinearities, and it is derived from Hamilton's principle. Then, the Galerkin decomposition technique is adopted to discretize the nonlinear partial differential equation into a nonlinear ordinary differential equation. This is solved analytically according to a multiple time scale method. A comprehensive parametric analysis was conducted to assess the influence of CNT volume fraction, beam slenderness, Mach number, and thickness ratio on the fundamental frequency and lateral dynamic deflection. Results indicate that FG-X reinforcement yields the highest frequency response and lateral deflection, followed by UD and FG-A patterns, whereas FG-O consistently exhibits the lowest performance metrics. An increase in CNT volume fraction and a reduction in slenderness ratio enhance the system's stiffness and frequency response up to a critical threshold, beyond which a damped beating phenomenon emerges. Moreover, higher Mach numbers and greater thickness ratios significantly amplify both frequency response and lateral deflections, although damping rates tend to decrease. These findings provide valuable insights into the optimization of CNTR composite structures for advanced aeroelastic applications under supersonic conditions, as useful for many engineering applications.

Keywords: carbon nanotubes; Euler–Bernoulli beam theory; modified third-order piston theory; multiple time scale method; nonlinear vibration; supersonic flow; Von Kármán nonlinearity

Academic Editor: Jordi Puiggali

Received: 10 June 2025
Revised: 30 July 2025
Accepted: 4 August 2025
Published: 6 August 2025

Citation: Alimoradzadeh, M.; Tornabene, F.; Dimitri, R. Aeroelastic Oscillations of Cantilever Beams Reinforced by Carbon Nanotubes Based on a Modified Third-Order Piston Theory. *Appl. Sci.* **2025**, *15*, 8700. https://doi.org/10.3390/app15158700

1. Introduction

In recent decades, the increased requirements of mechanical and physical performances in sustainable structures have favored the use of carbon nanotubes (CNTs) as reinforcement phase in composite materials, combined with the concept of functional graduation of materials to yield smooth and continuous characteristics [1–5]. Among different composite reinforcements, CNTs offer outstanding mechanical properties in terms of stiffness, strength, and mass density. The addition of only 1% of CNTs in the composite material,

for example, provides an increased elasticity modulus of about 40%, with a ductility reduction, an increased fracture toughness [6], and improved damping properties [7]. Among composite applications, like rotocrafts, robotic manipulators, or wind turbine blades, many structural components, like beams, plates, and shells, can be subjected to aerodynamic loadings, with the introduction of structural instabilities, e.g., flutter and divergence, with possible catastrophic effects. In most cases, the vibration amplitudes are large, making various forms of nonlinearity significant and situating the problem within the domain of nonlinear structural dynamics [8]. The dynamic behavior of flapping beams, for example, is expected to exhibit many complex phenomena commonly associated with nonlinear systems—such as bifurcations, quasi-periodicity, and chaos [8–10] and more specifically, those seen in nonlinear beam dynamics [11–16]. In such a context, in recent decades, an increased attention has been devoted to understanding the nonlinear structural dynamics through both numerical simulations and experimental studies. The mathematical and computational models employed in these investigations span a wide range of complexity—from finite element models of geometrically exact, curved composite beams [17] to simplified, single-mode representations capturing chaotic vibrations in beams with nonlinear boundary conditions [13]. The research on nonlinear dynamics, and particularly in the area of beam dynamics, is quite extensive, but more comprehensive discussions can be found in references [11,18] for general nonlinear dynamics, [9] for nonlinear vibrations, and [19] for nonlinear beam vibrations. It is well known from the literature that nonlinear systems can exhibit a wide variety of resonance phenomena, influenced by factors such as the strength of nonlinearity, the system's degrees of freedom, and the characteristics of the external excitation [20]. Thus, extensive studies have been conducted on the primary and superharmonic resonance behaviors of fundamental nonlinear systems, such as the Duffing oscillator, with particular attention to stability characteristics and the influence of key system parameters [21–23]. Rahman and Burton [22], for instance, compared second-order multiple scales perturbation techniques with numerical time integration to analyze the steady-state response and stability near the third-order superharmonic resonance. Their findings indicated that second-order perturbation results closely mirrored those from the first-order analysis and only modestly aligned with numerical outcomes. More recently, Dai et al. [24] employed a time-spectral approach to investigate the complex response behavior of the Duffing system, particularly focusing on the third-order superharmonic regime. Their analysis detailed the emergence of multi-valued response branches and jump phenomena, examined how harmonic components varied with frequency, and evaluated the roles of damping and excitation amplitude on the overall response landscape. In addition to these theoretical investigations, different computational strategies have been increasingly employed in the literature to study the aeroelastic behavior of various structural members. Among the recent works, a classical finite approach was proposed in refs. [25,26] to study the aeroelastic response of isotropic panels under different boundary conditions, or the flutter properties of functionally graded (FG) panels in supersonic airflow. Similarly, in Refs. [27–29], the authors studied the flutter behavior of damped composite plates [10], the lattice sandwich beams under a supersonic airflow [28], and the aerothermoelastic behavior of buckled cylindrical composite shells [29].

Alternatively, a cell-based smoothed finite element method was proposed by Natarajan et al. [30,31] to assess the flutter response of FG panels in the presence or absence of cracks, whereas a Galerkin method was applied by Kouchakzadeh et al. [32] for the flutter study of laminated composite panels. The Galerkin decomposition technique was combined to the multiple time scale method (MTS) in Ref. [33], to solve numerically the nonlinear partial differential equation of the problem, whereas a p-version finite element method (p-FEM) was combined to the third-order shear deformation theory in Ref. [34] for the aeroelastic

analyses of laminated hybrid multiscale composite plates, under a supersonic airflow. Various applications of finite strain-based theories have been presented in Refs. [35–40] to analyze the superharmonic and subharmonic resonances of composite beams exposed to thermal environments and subjected to moving mass loads. In parallel, more recent investigations have concentrated on the flutter instability phenomena in composite beams [41,42] and plates [43,44], utilizing approaches such as the Galerkin method and the differential quadrature method. These studies consistently incorporate geometric nonlinearities within their theoretical frameworks, as exemplified in Ref. [45], which explores the nonlinear axial-lateral vibration behavior of functionally graded, fiber-reinforced composite laminated cantilever beams under combined aerodynamic and thermal loading conditions.

Starting with the main idea from this last reference, the present work aims at extending the study to the nonlinear aeroelastic oscillations of CNT-based cantilever beams, by employing a modified third-order piston theory and the von Kármán geometrical nonlinearities, whose nonlinear governing equation is solved in discrete form, based on the Galerkin decomposition and MTS methods. A numerical investigation evaluates systematically the sensitivity of the dynamic response of the composite beam-like structure to the reinforcement patterns and volume fraction, but also to the free air velocity, Mach number, slenderness ratio, and thickness ratio. The structure of the paper is as follows: after this literature review, the theoretical framework of the problem is presented in Section 2, with the corresponding numerical formulation detailed in Section 3. Section 4 discusses the numerical results, and concluding remarks are provided in Section 5.

2. Theoretical Problem

Let us consider a straight carbon nanotube reinforced composite (CNTRC) cantilever beam of length L, thickness h, and width b, in the x, y and z direction, respectively, subjected to supersonic air flow, as shown in Figure 1. As shown in Figure 1, we assume three different patterns of reinforcement in the thickness direction, namely, a uniform distribution (*UD*), and two different functionally distributions, i.e., *FG-O* and *FG-X*, respectively. In addition, it is assumed that the *SWCNTs* are embedded within an isotropic polymer matrix without any abrupt interface in the overall region of the beam.

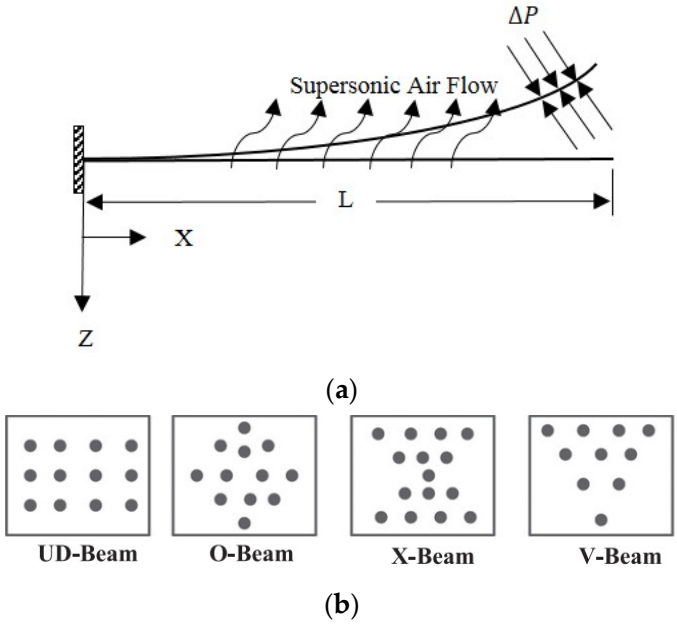

Figure 1. Geometrical and mechanical model of the CNTR composite cantilever beam. (**a**) Geometrical scheme. (**b**) Cross sections of different reinforcement patterns.

The rule of mixtures is applied to describe the effective material properties of the *CNTRC* beams, i.e., the elasticity modulus E, the shear modulus G, the Poisson's ratio υ, and the density ρ [29,30]

$$E_{11} = \eta_1 V_{CNT} E_{11}^{CNT} + V_p E^p \tag{1}$$

$$\frac{\eta_2}{E_{22}} = \frac{V_{CNT}}{E_{22}^{CNT}} + \frac{V_p}{E^p} \tag{2}$$

$$\frac{\eta_3}{G_{12}} = \frac{V_{CNT}}{G_{12}^{CNT}} + \frac{V_p}{G^p} \tag{3}$$

$$V_{CNT} + V_p = 1 \tag{4}$$

$$v = V_{CNT} v^{CNT} + V_p v^p \tag{5}$$

$$\rho = V_{CNT} \rho^{CNT} + V_p \rho^p \tag{6}$$

where superscripts CNT and p refer to the material properties of carbon nanotubes and polymer matrix. Moreover, η_1, η_2, η_3 denote the *CNTs* efficiency parameters, whereas V_p and V_{CNT} define the volume fractions for the polymer matrix and *CNT*, respectively. Table 1 represents the variation in the *CNTs* volume fractions with the thickness direction for different patterns [46].

Table 1. Volume fractions of CNTs as a function of thickness direction for different distributions of ***CNTs*** [46].

Patterns of *CNTs*	V_{CNT}
UD	V_{CNT}^*
FG-A	$V_{CNT}^*\left(1 - \frac{2z}{h}\right)$
FG-O	$2V_{CNT}^*\left(1 - 2\frac{\lvert z\rvert}{h}\right)$
FG-X	$4V_{CNT}^*\frac{\lvert z\rvert}{h}$

In this table, V_{CNT}^* is a fixed volume fraction of *CNTs*, where the following efficiency parameters for *CNTs* are considered, for three different assumptions for V_{CNT}^*, as [47]

$$\eta_1 = 0.137, \eta_2 = 1.022, \eta_3 = 0.715 \quad \text{for} \quad V_{CNT}^* = 0.12 \tag{7}$$

$$\eta_1 = 0.142, \eta_2 = 1.626, \eta_3 = 1.138 \quad \text{for} \quad V_{CNT}^* = 0.17 \tag{8}$$

$$\eta_1 = 0.141, \eta_2 = 1.585, \eta_3 = 1.109 \quad \text{for} \quad V_{CNT}^* = 0.28 \tag{9}$$

The Euler–Bernoulli beam theory is here assumed to define the displacement field of an arbitrary point in the beam along the x, y, and z direction denoted by $u_x(x,\ z,\ t)$, $u_y(x,\ z,\ t)$ and $u_z(x,\ z,\ t)$, respectively, as follows [48]:

$$u_x = u(x,t) - z\frac{\partial w(x,t)}{\partial x} \tag{10}$$

$$u_y = 0 \tag{11}$$

$$u_z = w(x,t) \tag{12}$$

with u and w the axial and lateral displacement of the midplane in the x and z direction, respectively, and $\partial w(x,t)/\partial x$ is the rotation angle about the y axis of the cross-section at

time t. The nonlinear kinematic relations are defined according to the following nonzero components of the Von Kármán strain tensor [49]:

$$\varepsilon_{xx} = \frac{\partial u_x}{\partial x} + \frac{1}{2}\left(\frac{\partial u_z}{\partial x}\right)^2 \tag{13}$$

$$\varepsilon_{xz} = \varepsilon_{zx} = \frac{1}{2}\left[\frac{\partial u_x}{\partial z} + \frac{\partial u_z}{\partial x}\right] \tag{14}$$

By substitution of Equations (10) and (12) into Equations (13) and (14) we get

$$\varepsilon_{xz} = \varepsilon_{xz} = 0 \tag{15}$$

$$\varepsilon_{xx} = \frac{\partial u}{\partial x} - z\frac{\partial^2 w}{\partial x^2} + \frac{1}{2}\left(\frac{\partial w}{\partial x}\right)^2 \tag{16}$$

The strain energy is defined as follows [47]:

$$U_S = \frac{1}{2}\int_0^L \int_A (\sigma_{xx}\varepsilon_{xx} + \sigma_{xz}\varepsilon_{xz}) dA dx \tag{17}$$

where σ_{xx} and σ_{xz} are the normal and shear stress components, respectively, and can be expressed as follows [50]:

$$\sigma_{xx} = \frac{E_{11}(z)}{1 - \vartheta^2(z)}\varepsilon_{xx} \tag{18}$$

$$\sigma_{xz} = G_{12}(z)\varepsilon_{xz} \tag{19}$$

Based on Equations (15)–(19), the strain energy of the CNTRC beam is defined as follows:

$$U_s = \frac{b}{2}\int_0^L \left\{ A_{11}\left(\frac{\partial u}{\partial x} + \frac{1}{2}\left(\frac{\partial w}{\partial x}\right)^2\right)^2 + D_{11}\left(\frac{\partial^2 w}{\partial x^2}\right)^2 - B_{11}\frac{\partial^2 w}{\partial x^2}\left(2\frac{\partial u}{\partial x} + \left(\frac{\partial w}{\partial x}\right)^2\right)\right\} dx \tag{20}$$

where

$$\int_{-\frac{h}{2}}^{\frac{h}{2}} \frac{E_{11}(z)}{1 - \vartheta^2(z)}\left(1, z, z^2\right) dz = A_{11}, B_{11}, D_{11} \tag{21}$$

As discussed before, the beam is subjected to an aerodynamic force perpendicular to its surface, ΔP, because of the supersonic air flow. The unsteady aerodynamic load is expressed by a modified third-order piston theory as follows [51]:

$$\Delta P = -\zeta\left(\frac{\partial w}{\partial t} + u_\infty \frac{\partial w}{\partial x}\right)\left[1 + \xi\left(\frac{\partial w}{\partial x}\right)^2\right] \tag{22}$$

where

$$\zeta = 2\frac{\rho_\infty u_\infty}{M_\infty} \tag{23}$$

$$\xi = \frac{M_\infty^2(1+\gamma)}{12} \tag{24}$$

where ρ_∞, u_∞, and M_∞, are the density, velocity, and Mach number of the free stream air flow, respectively. Moreover, γ is the specific-heat ratio of the air $(\gamma \cong 1.4)$. The virtual work associated with the external forces, W, and the kinetic energy, K, of the beam can be expressed as follows [49]:

$$W = \int_A \Delta P w(x,t) dA \tag{25}$$

$$K = \frac{1}{2}\int_{Vol}\rho(z)\left[\left(\frac{\partial u_x}{\partial t}\right)^2 + \left(\frac{\partial u_y}{\partial t}\right)^2 + \left(\frac{\partial u_z}{\partial t}\right)^2\right]dV \tag{26}$$

where A stands for the surface area of the beam. By substitution of Equations (10)–(12) into Equation (26) we get

$$K = \frac{b}{2}\int_0^L \left\{ I_0\left[\left(\frac{\partial u}{\partial t}\right)^2 + \left(\frac{\partial w}{\partial t}\right)^2\right] + I_2\left(\frac{\partial^2 w}{\partial x \partial t}\right)^2 - 2I_1\left(\frac{\partial u}{\partial t}\frac{\partial^2 w}{\partial x \partial t}\right)\right\}dx \tag{27}$$

where

$$\int_{-\frac{h}{2}}^{\frac{h}{2}} \rho(z)\left(1, z, z^2\right)dz = I_0, I_1, I_2 \tag{28}$$

The Hamilton principle is here applied to determine the nonlinear partial differential equation governing the motion, i.e., [49]

$$\delta\int_{t_1}^{t_2}[\mathrm{K} - \mathrm{U_s} + \mathrm{W}]\mathrm{dt} - 0 \tag{29}$$

where δ denotes the variational notation. Substituting Equations (20), (25), and (27) into Equation (29) leads to the following nonlinear partial differential equation governing the motion of the *CNTRC* beams:

$$\frac{\partial}{\partial x}\left[A_{11}\left(\frac{\partial u}{\partial x} + \frac{1}{2}\left(\frac{\partial w}{\partial x}\right)^2\right) - B_{11}\frac{\partial^2 w}{\partial x^2}\right] = I_0\frac{\partial^2 u}{\partial t^2} - I_1\frac{\partial^3 w}{\partial x \partial t^2} \tag{30}$$

$$\begin{aligned} I_0\tfrac{\partial^2 w}{\partial t^2} + \tfrac{\partial}{\partial x}\left[I_1\tfrac{\partial^2 u}{\partial t^2} - I_2\tfrac{\partial^3 w}{\partial x \partial t^2}\right] + \tfrac{\partial^2}{\partial x^2}\left[D_{11}\tfrac{\partial^2 w}{\partial x^2} - B_{11}\left(\tfrac{\partial u}{\partial x} + \tfrac{1}{2}\left(\tfrac{\partial w}{\partial x}\right)^2\right)\right] \\ - \tfrac{\partial}{\partial x}\left[A_{11}\left(\tfrac{\partial u}{\partial x} + \tfrac{1}{2}\left(\tfrac{\partial w}{\partial x}\right)^2\right) - B_{11}\tfrac{\partial^2 w}{\partial x^2}\right]\tfrac{\partial w}{\partial x} \\ - \tfrac{\partial^2 w}{\partial x^2}\left[A_{11}\left(\tfrac{\partial u}{\partial x} + \tfrac{1}{2}\left(\tfrac{\partial w}{\partial x}\right)^2\right) - B_{11}\tfrac{\partial^2 w}{\partial x^2}\right] = \Delta P \end{aligned} \tag{31}$$

By ignoring the axial inertia, and the rotational inertia, Equations (30) and (31) take the following form [52]:

$$\frac{\partial}{\partial x}\left[A_{11}\left(\frac{\partial u}{\partial x} + \frac{1}{2}\left(\frac{\partial w}{\partial x}\right)^2\right) - B_{11}\frac{\partial^2 w}{\partial x^2}\right] = 0 \tag{32}$$

$$\begin{aligned} I_0\tfrac{\partial^2 w}{\partial t^2} + \tfrac{\partial^2}{\partial x^2}\left[D_{11}\tfrac{\partial^2 w}{\partial x^2} - B_{11}\left(\tfrac{\partial u}{\partial x} + \tfrac{1}{2}\left(\tfrac{\partial w}{\partial x}\right)^2\right)\right] \\ - \tfrac{\partial^2 w}{\partial x^2}\left[A_{11}\left(\tfrac{\partial u}{\partial x} + \tfrac{1}{2}\left(\tfrac{\partial w}{\partial x}\right)^2\right) - B_{11}\tfrac{\partial^2 w}{\partial x^2}\right] - \Delta P \\ - \tfrac{\partial}{\partial x}\left[A_{11}\left(\tfrac{\partial u}{\partial x} + \tfrac{1}{2}\left(\tfrac{\partial w}{\partial x}\right)^2\right) - B_{11}\tfrac{\partial^2 w}{\partial x^2}\right]\tfrac{\partial w}{\partial x} = 0 \end{aligned} \tag{33}$$

Equation (32) can be redefined as follows:

$$\frac{\partial^2 u}{\partial x^2} = \frac{\partial}{\partial x}\left[-\frac{1}{2}\left(\frac{\partial w}{\partial x}\right)^2 + \frac{B_{11}}{A_{11}}\frac{\partial^2 w}{\partial x^2}\right] \tag{34}$$

which is integrated with respect to the x-axis to yield

$$\frac{\partial u}{\partial x} = -\frac{1}{2}\left(\frac{\partial w}{\partial x}\right)^2 + \frac{B_{11}}{A_{11}}\frac{\partial^2 w}{\partial x^2} - \frac{N_0(t)}{A_{11}} \tag{35}$$

The integration of Equation (35) leads to

$$u = \int_0^x -\frac{1}{2}\left(\frac{\partial w}{\partial x}\right)^2 dx + \frac{B_{11}}{A_{11}}\frac{\partial w}{\partial x} - \frac{N_0 x}{A_{11}} + N_1(t) \tag{36}$$

For the cantilever beam, the following boundary condition can be considered [53]

$$u = 0, w = 0, \frac{\partial w}{\partial x} = 0 \qquad \text{at} \qquad x = 0 \tag{37}$$

$$\frac{\partial u}{\partial x} = 0, \frac{\partial^2 w}{\partial x^2} = 0, \frac{\partial^3 w}{\partial x^3} = 0 \quad \text{at} \quad x = L \tag{38}$$

Using Equations (35)–(38) yields

$$\frac{N_0}{A_{11}} = -\frac{1}{2}\left(\frac{\partial w(L,t)}{\partial x}\right)^2 + \frac{B_{11}}{A_{11}}\left(\frac{\partial^2 w(L,t)}{\partial x^2}\right) \tag{39}$$

$$N_1(t) = -\frac{B_{11}}{A_{11}}\frac{\partial w(0,t)}{\partial x} \tag{40}$$

By substitution of Equations (32) and (35) into Equation (33), we obtain the following nonlinear differential equation of motion:

$$I_0\frac{\partial^2 w}{\partial t^2} + \left(D_{11} - \frac{{B_{11}}^2}{A_{11}}\right)\frac{\partial^4 w}{\partial x^4} + N_0\frac{\partial^2 w}{\partial x^2} = \Delta P \tag{41}$$

where $N_0(t)$ is defined in Equation (39).

3. Numerical Solution

The Galerkin method is here applied to derive the ordinary differential equation of motion from Equation (41), such that the solution can be determined as follows [54]:

$$w(x,t) = \sum_{n=1}^{\infty} \psi_n(x) \cdot q_n(t) \tag{42}$$

where $\psi_n(x)$ and $q_n(t)$ refers to the n-th mode shape function (admissible function) and n-th modal coefficient, respectively. Considering the most dominant mode of the beam, i.e., the first mode, the solution of Equation (41) can be expressed as follows [54]:

$$w(x,t) = \psi(x) \cdot q(t) \tag{43}$$

For a cantilever beam, the mode shape function is defined as follows [54]:

$$\psi(x) = (cos\beta x - cosh\beta x) - \frac{cos\beta l + cosh\beta l}{sin\beta l + sinh\beta l}(sin\beta x - sinh\beta x), \quad \beta l = 1.8751 \tag{44}$$

which satisfies the boundary conditions in Equations (37) and (38). Substituting Equation (43) into Equation (41) yields

$$I_0\psi\ddot{q} + \left[c_0 + c_1 q^2\right]\dot{q} + a_1 q + a_2 q^2 + a_3 q^3 = 0 \tag{45}$$

$\dot{q}(t)$ and $\ddot{q}(t)$ are the first and the second derivative of $q(t)$ with respect to time. Also, the nonlinear coefficients c_0, c_1, a_1, a_2, and a_3 are defined in terms of the stiffness

parameters A_{11}, B_{11}, D_{11}, together with the mode shape function ψ and its derivatives ψ_x, ψ_{xx}, and ψ_{xxxx},

$$a_1 = \left[\psi_{xxxx}\left(D_{11} - \frac{{B_{11}}^2}{A_{11}}\right) + \zeta u_\infty \psi_x\right] \tag{46}$$

$$a_2 = B_{11}\psi_{xx}\psi_{xx}(L) \tag{47}$$

$$a_3 = \zeta\xi u_\infty \psi_x^3 - \frac{A_{11}}{2}\psi_{xx}(\psi_x(L))^2 \tag{48}$$

$$c_0 = \zeta\psi, c_1 = \zeta\xi\psi\psi_x^2 \tag{49}$$

where ψ_x, ψ_{xx}, and ψ_{xxxx}, refer to the first-, second-, and fourth-order derivative of $\psi(x)$ with respect to x, respectively, By multiplying Equation (45) with a mode shape function $\psi(x)$ and the integration over the domain $(0, L)$ gets to the following nonlinear ordinary differential equation:

$$\ddot{q} + \left(2\hat{\mu}_0 + \hat{\mu}_1 q^2\right)\dot{q} + \omega_0^2 q + \hat{\eta}_2 q^2 + \hat{\eta}_3 q^3 = 0 \tag{50}$$

where $\hat{\mu}_0, \hat{\mu}_1, \omega_0^2, \hat{\eta}_2$, and $\hat{\eta}_3$ are defined as follows:

$$\hat{\mu}_0 = \frac{1}{2}\frac{\int_0^L c_0\psi(x)dx}{\int_0^L I_0\psi^2(x)dx} \tag{51}$$

$$\hat{\mu}_1 = \frac{\int_0^L c_1\psi(x)dx}{\int_0^L I_0\psi^2(x)dx} \tag{52}$$

$$\omega_0^2 = \frac{\int_0^L a_1\psi(x)dx}{\int_0^L I_0\psi^2(x)dx} \tag{53}$$

$$\hat{\eta}_2 = \frac{\int_0^L a_2\psi(x)dx}{\int_0^L I_0\psi^2(x)dx} \tag{54}$$

$$\hat{\eta}_3 = \frac{\int_0^L a_3\psi(x)dx}{\int_0^L I_0\psi^2(x)dx} \tag{55}$$

The nonlinear ordinary differential Equation (50) can be solved by using the MTS method [8], under the following assumption:

$$\hat{\mu}_0 = \epsilon^2\mu_0 \tag{56}$$

being $\epsilon \ll 1$, a dimensionless parameter acting as a bookkeeping parameter. By substituting Equation (56) into Equation (50), we get

$$\ddot{q} + \left(2\epsilon^2\mu_0 + \hat{\mu}_1 q^2\right)\dot{q} + \omega_0^2 q + \hat{\eta}_2 q^2 + \hat{\eta}_3 q^3 = 0 \tag{57}$$

We now introduce the independent time variables as follows [55]:

$$T_n = \epsilon^n t, n = 0, 1, 2, 3, \ldots \tag{58}$$

Therefore, the derivatives with respect to the time it takes the following form due to the chain rule:

$$\frac{d}{dt} = D_0 + \epsilon D_1 + \epsilon^2 D_2 + \epsilon^3 D_3 + \cdots \tag{59}$$

$$\frac{d^2}{dt^2} = D_0^2 + 2\epsilon D_0 D_1 + \epsilon^2\left(D_1^2 + 2D_0 D_2\right) + 2\epsilon^3(D_1 D_2) + \cdots \tag{60}$$

where

$$D_i = \frac{\partial}{\partial T_i}, i = 0, 1, 2, 3, \ldots \tag{61}$$

Following the MTS method, the solution of Equation (57) can be expressed as follows [8]:

$$q = \epsilon q_1(T_0, T_1, T_2) + \epsilon^2 q_2(T_0, T_1, T_2) + \epsilon^3 q_3(T_0, T_1, T_2) + \ldots \tag{62}$$

Substituting Equation (62) into Equation (57) combined with Equations (58)–(60), and by equating the coefficients of similar power of ϵ to zero yields

$$\left(D_0^2 + \omega_0^2\right) q_1 = 0 \tag{63}$$

$$\left(D_0^2 + \omega_0^2\right) q_2 = -2D_0 D_1 q_1 - \hat{\eta}_2 q_1^2 \tag{64}$$

$$\left(D_0^2 + \omega_0^2\right) q_3 = -2D_0 D_1 q_2 - \hat{\eta}_3 q_1^3 - \hat{\mu}_1 q_1^2 D_0 q_1 - \left(D_1^2 + 2D_0 D_2\right) q_1 - 2\mu_0 D_0 q_1 - 2\hat{\eta}_2 q_1 q_2 \tag{65}$$

whose general solution can be defined as follows:

$$q_1 = A(T_1, T_2) e^{i\omega_0 T_0} + \overline{A}(T_1, T_2) e^{-i\omega_0 T_0} \tag{66}$$

$A(T_1, T_2)$ being an unknown complex function. It can be determined by eliminating the secular terms from q_2 and q_3. At the same time, $\overline{A}(T_1, T_2)$ is the complex conjugate of A. The substitution of Equation (66) into Equation (64) yields

$$\left(D_0^2 + \omega_0^2\right) q_2 = -2i\omega_0 D_1 A e^{i\omega_0 T_0} - \hat{\eta}_2\left[A^2 e^{2i\omega_0 T_0} + A\overline{A}\right] + cc \tag{67}$$

cc is the complex conjugate of the preceding terms. The secular terms are simplified from q_2 by equating the coefficients of $e^{\pm i\omega_0 T_0}$ to zero as follows:

$$D_1 A(T_1, T_2) = 0 \tag{68}$$

Therefore, it is

$$= A(T_2) \tag{69}$$

Based on Equation (68), the particular solution of Equation (67) is defined as follows:

$$q_2 = \frac{\hat{\eta}_2}{3\omega_0^2}\left[A^2 e^{2i\omega_0 T_0} - 3A\overline{A}\right] + cc \tag{70}$$

Bu substituting Equations (66) and (70) into Equation (65) yields

$$\begin{aligned}\left(D_0^2 + \omega_0^2\right) q_3 = \; & -\left[\hat{\mu}_1 i\omega_0 + \frac{2\hat{\eta}_2^2}{3\omega_0^2} + \hat{\eta}_3\right] A^3 e^{3i\omega_0 T_0} \\ & + \left[A^2\overline{A}\left(\frac{10\hat{\eta}_2^2 - 9\omega_0^2\hat{\eta}_3}{3\omega_0^2}\right) - 2i\omega_0(D_2 A + \mu_0 A\right. \\ & \left. + \tfrac{1}{2}\hat{\mu}_1 A^2\overline{A}\right)] e^{i\omega_0 T_0} + cc\end{aligned} \tag{71}$$

The secular terms are simplified from q_3 by equating to zero the coefficients of $e^{\pm i\omega_0 T_0}$ in Equation (71), as follows:

$$-2i\omega_0\left(D_2A+\mu_0A+\frac{1}{2}\hat{\mu}_1A^2\overline{A}\right)+A^2\overline{A}\left(\frac{10\hat{\eta}_2^2-9\omega_0^2\hat{\eta}_3}{3\omega_0^2}\right)=0 \tag{72}$$

where $A(T_2)$ is defined in polar form as follows [8]:

$$A=\frac{1}{2}ae^{i\beta} \tag{73}$$

a and β being real functions of T_2. By substituting Equation (73) into Equation (72) and by separating results into their real and imaginary parts leads to

$$\frac{da}{dT_2}=-\mu_0a-\frac{1}{8}\hat{\mu}_1a^3 \tag{74}$$

$$\frac{da}{dT_2}=-\mu_0a-\frac{1}{8}\hat{\mu}_1a^3 \tag{75}$$

Solving Equation (74) yields

$$a^2=\frac{8}{\frac{\hat{\mu}_1}{\mu_0}\left[a_0e^{2\mu_0T_2}-1\right]} \tag{76}$$

whereas, the substitution of Equation (76) into Equation (75) leads to

$$\beta=L_n\left[\frac{a_0e^{2\mu_0T_2}-1}{a_0e^{2\mu_0T_2}}\right]^{\Omega}+\beta_0 \tag{77}$$

where

$$\Omega=\frac{9\omega_0^2\hat{\eta}_3-10\hat{\eta}_2^2}{6\hat{\mu}_1\omega_0^3} \tag{78}$$

and a_0, β_0 are constants of integration. The motion starts under the following initial conditions

$$a(0)=\frac{\Lambda}{\epsilon},\qquad \beta(0)=0 \tag{79}$$

The combination of Equations (76)–(79) together with Equations (56) and (58) leads to the following expressions for a and β:

$$a=\sqrt{\frac{8}{\frac{\epsilon^2\hat{\mu}_1}{\hat{\mu}_0}\left(a_0e^{2\hat{\mu}_0t}-1\right)}} \tag{80}$$

$$\beta=L_n\left[\frac{a_0e^{2\hat{\mu}_0t}-1}{(a_0-1)e^{2\hat{\mu}_0t}}\right]^{\Omega} \tag{81}$$

where

$$a_0=1+\frac{8\hat{\mu}_0}{\hat{\mu}_1\Lambda^2} \tag{82}$$

By substituting Equations (66), (70) and (73) into Equation (62) leads to

$$q=\epsilon a\cos\Theta(t)-\epsilon^2a^2\frac{\hat{\eta}_2}{2\omega_0^2}\left[1-\frac{1}{3}\cos 2\Theta(t)\right] \tag{83}$$

where

$$(t) = \omega_0 t + \beta \tag{84}$$

Finally, the substitution of Equation (80) into Equation (83) yields to the following semi-analytical response:

$$q = \sqrt{\frac{8}{\frac{\hat{\mu}_1}{\hat{\mu}_0}\left(a_0 e^{2\hat{\mu}_0 t} - 1\right)}} cos\,\Theta - \frac{4\hat{\eta}_2}{\frac{\hat{\mu}_1}{\hat{\mu}_0}\omega_0^2\left(a_0 e^{2\hat{\mu}_0 t} - 1\right)}\left[1 - \frac{1}{3}cos\,2\Theta(t)\right] + O\left(\epsilon^3\right) \tag{85}$$

where a_0 is defined in Equation (82).

4. Parametric Investigation

A numerical investigation of the nonlinear oscillation for the selected structural components subjected to aero-elastic load is herein performed based on a modified third-order piston theory, and the following assumptions: $\rho_\infty = 1.29\left(\frac{kg}{m^3}\right)$, $190\left(\frac{m}{s}\right) \leq u_\infty \leq 300\left(\frac{m}{s}\right)$, and $2 \leq M_\infty \leq 6$. The CNTRC beam is characterized by the following geometric and material properties at 300 k [36]: $L = 1.2$ m, $b = 0.15$ m, $h = 0.01$ m, $\Lambda = 0.001$ m, $E_{11}^{CNT} = 5.6466$ TPa, $E_{22}^{CNT} = 7.0800$ TPa, $G_{12}^{CNT} = 1.9445$ TPa, $v^{CNT} = 0.175$, $\rho^{CNT} = 1400$ kg/m^3, $E^p = 3.52$ GPa, $v^p = 0.34$, and $\rho^p = 1150$ kg/m^3.

The numerical analysis starts by evaluating the accuracy of the proposed method, based on a comparative study against the literature. To this end, the fundamental frequencies of a homogeneous cantilever beam (made of pure polymer) are computed in Table 2 for different values of slenderness ratio, while comparing them with Ref. [53] based on a simple Euler–Bernoulli beam theory. From Table 2, it is worth noticing that the current results match accurately predictions from Ref. [53], confirming the expected accuracy of the method here proposed.

Table 2. Comparative results for fundamental frequencies of a cantilever beam. ($u_\infty = 0$).

$\frac{L}{h}$	*Fundamental Frequency* $\omega_L(\frac{rad}{s})$		
	Present Work		
	ϑ**=0**	$\vartheta \neq$**0**	**Rao [53]**
25.0	302.1178	284.1192	284.1192
50.0	75.5294	71.0298	71.0298
75.0	33.5686	31.5688	31.5688
90.0	23.3116	21.9228	21.9228
100.0	18.8824	17.7575	17.7575
120.0	13.1128	12.3316	12.3316

In Figure 2, we illustrate the variation in the fundamental frequency as a function of the slenderness ratio for different CNT reinforcement patterns. It is evident that the fundamental frequency decreases significantly with increasing slenderness ratio, particularly for values below 60, due to the reduced structural stiffness. Among the reinforcement schemes,

the FG-X pattern demonstrates the highest frequency response, followed by the UD and FG-A patterns. The FG-O configuration consistently yields the lowest frequency. This trend underscores the significant impact of reinforcement grading on dynamic stiffness and aeroelastic stability. At the same time, Figure 3 presents the influence of CNT volume fraction on the fundamental frequency for various slenderness ratios. An increase in the CNT volume fraction enhances the stiffness of the composite, which leads to a noticeable increase in the natural frequency. This effect is especially pronounced at lower slenderness ratios, where the structure is more sensitive to reinforcement distribution due to its greater susceptibility to bending. These findings confirm the critical role of CNT content in tailoring vibrational performance.

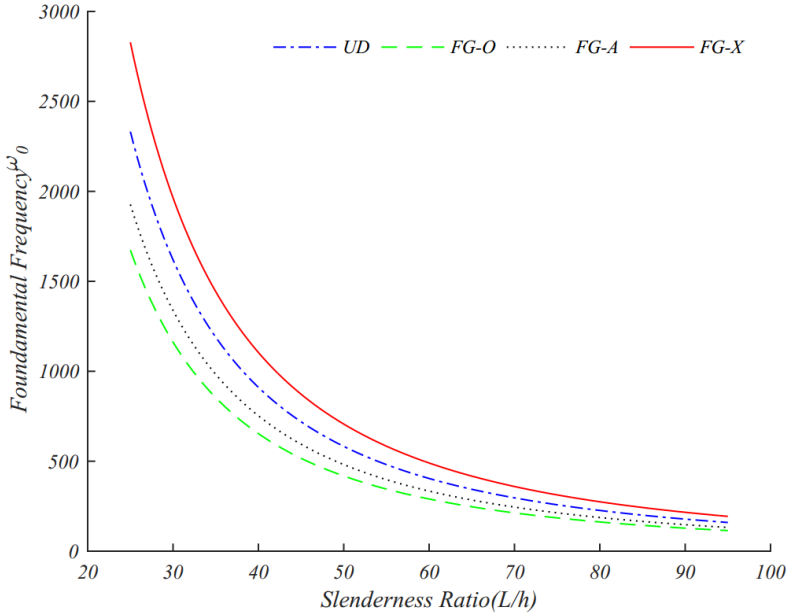

Figure 2. Variation in the fundamental frequency vs. slenderness ratio for different patterns. $V^*_{CNT} = 0.17$.

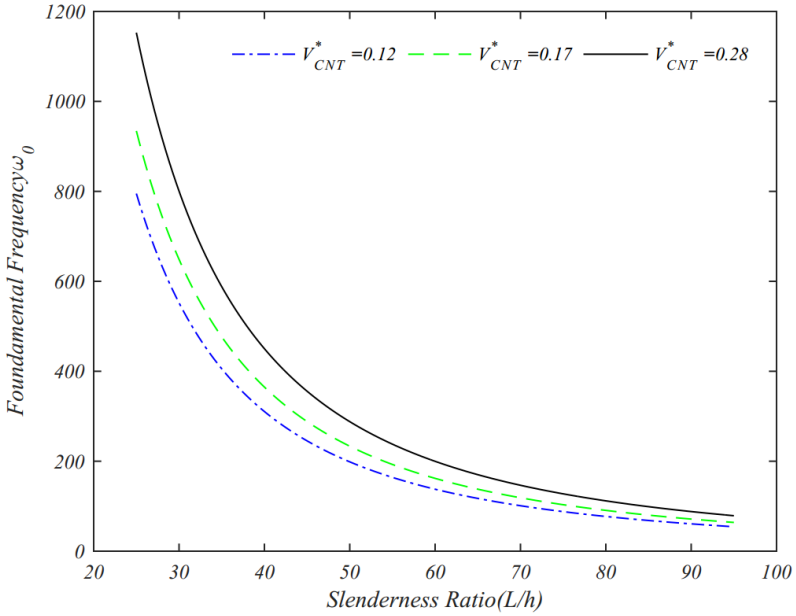

Figure 3. Variation in the fundamental frequency with the slenderness ratio for different volume fractions. $FG - X$ pattern.

Figure 4 shows the time history of the lateral dynamic displacement for beams with different reinforcement patterns under a supersonic airflow. The beam with a FG-X rein-

forcement exhibits the largest amplitude of oscillation and the highest vibration frequency, indicating a stiffer and more responsive structure. Conversely, the FG-O pattern results in the smallest dynamic deflection and the lowest frequency, confirming the inferior stiffness and dynamic performance of this configuration. The UD and FG-A beams show intermediate behavior, highlighting the tunability of aeroelastic characteristics through tailored CNT distributions.

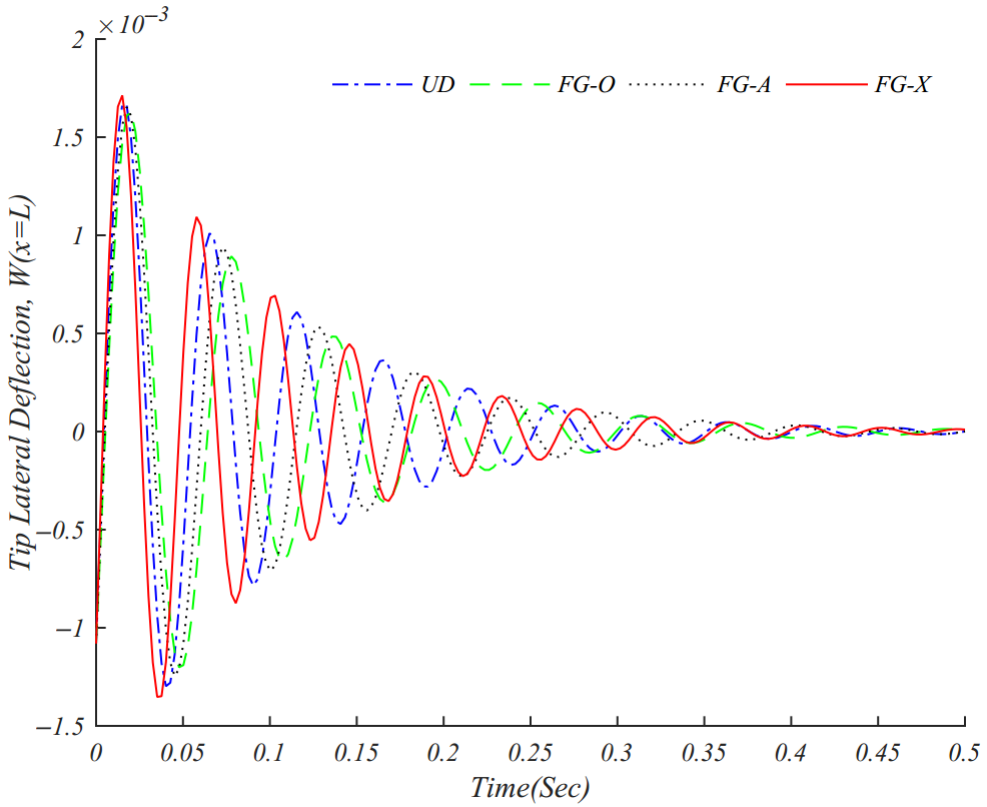

Figure 4. Time history of the system at different reinforcement patterns. $u_\infty = 190.0\left(\frac{m}{s}\right)$, $M_\infty = 2.0$, $V^*_{CNT} = 0.17$.

Moreover, Figure 5 shows the time history of the system for varying CNT volume fractions. As the volume fraction increases, both the frequency and amplitude of oscillations increase, a consequence of the enhanced material stiffness imparted by the CNT reinforcement. These results demonstrate the effectiveness of higher CNT content in increasing structural rigidity and improving resistance to aeroelastic instabilities. Another key aspect affecting the structural vibrations and oscillations is the free stream air velocity, as analyzed in the parametric time response of the beam in Figure 6, for different free stream air velocities. The results from this figure show that both the vibration frequency and lateral deflection increase with airspeed, suggesting that the aerodynamic loading amplifies the structural response. However, this amplification is relatively linear compared to more substantial changes observed with Mach number variations, as visible from Figure 7. In this last figure, indeed, a noticeable increase in both the frequency and amplitude of oscillations occurs as the Mach number rises, indicating a strong aerodynamic coupling. Compared to Figure 6, these results suggest that the Mach number exerts a more dominant influence than air velocity alone, due to nonlinear compressibility effects captured by the third-order piston theory. Figure 8 focuses on the influence of slenderness ratio on the nonlinear frequency response. As the slenderness ratio decreases (i.e., the beam becomes stubbier), the system becomes stiffer, leading to higher oscillation frequencies. However, beyond a certain threshold, the system exhibits a damped harmonic response with amplitude

modulation—a signature of beating phenomena. This indicates the proximity of the excitation frequency to the system's damped natural frequency, resulting in a complex dynamic behavior. As last parametric investigation, we assess the role of the thickness ratio on the time history response, as visible in Figure 9. Based on this figure, as the thickness ratio increases, the system clearly shows a marked increase in vibration frequency and dynamic stiffness. However, the damping rate diminishes, leading to larger amplitude oscillations and sustained lateral deflections. This behavior suggests a trade-off between increased stiffness and reduced damping, which must be carefully balanced in design applications involving high thickness ratios. While the proposed numerical model has been validated against classical theoretical results, the incorporation of experimental data from physical tests on CNT-reinforced beams under aeroelastic loading would be an important step to further substantiate the predictions. Due to the complexity and limited availability of such data under supersonic flow conditions, this remains an area of active investigation for future work. In addition, the current study has solely focused on aerodynamic forces and does not account for thermal effects. This simplification was made to isolate the influence of aerodynamic loads and structural parameters such as CNT volume fraction, slenderness, and thickness ratios under supersonic flow using the modified third-order piston theory.

However, we recognize the importance of thermal loads, especially in high-speed environments where significant temperature gradients can arise due to aerodynamic heating. As pointed out in Ref. [55], thermal stresses can considerably alter the stiffness and damping characteristics of composite structures, thereby influencing their vibration and stability behavior. These effects are particularly relevant for FG and thick composite beams, where thermal gradients can lead to significant stress redistribution across the thickness. Given the potential coupling between aerodynamic and thermal loads, a more complete aero-thermoelastic model would provide deeper insight into the dynamic behavior of CNT-reinforced composites. Therefore, we plan to extend this work in future studies by incorporating thermal effects using higher-order shear deformation theories (e.g., Timoshenko theory) to capture shear deformation and rotary inertia effects more accurately. This will allow us to model more realistic high-speed operating conditions and evaluate combined aerodynamic and thermal influences on nonlinear oscillation behavior.

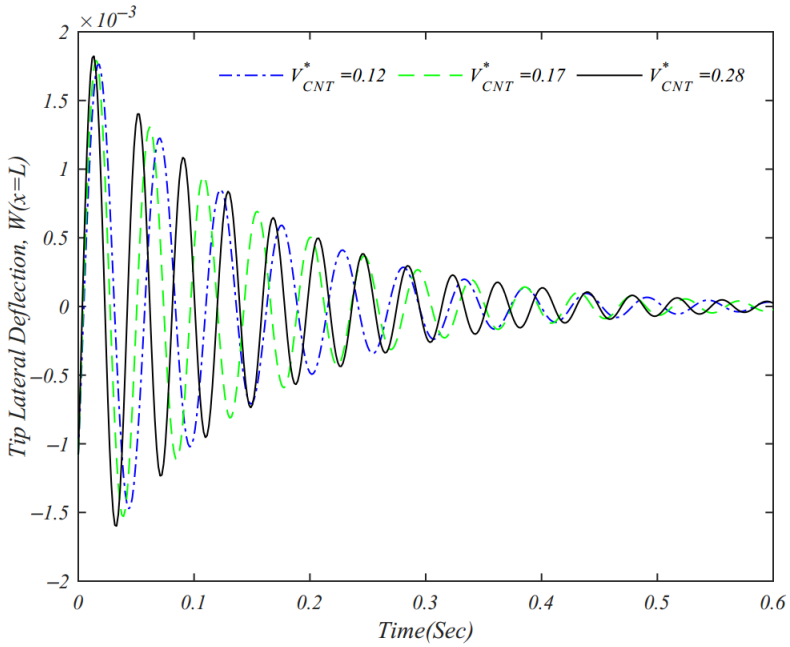

Figure 5. Time history of the system at different volume fractions. $u_\infty = 190.0\left(\frac{m}{s}\right)$, $M_\infty = 3.0$, $FG - X$.

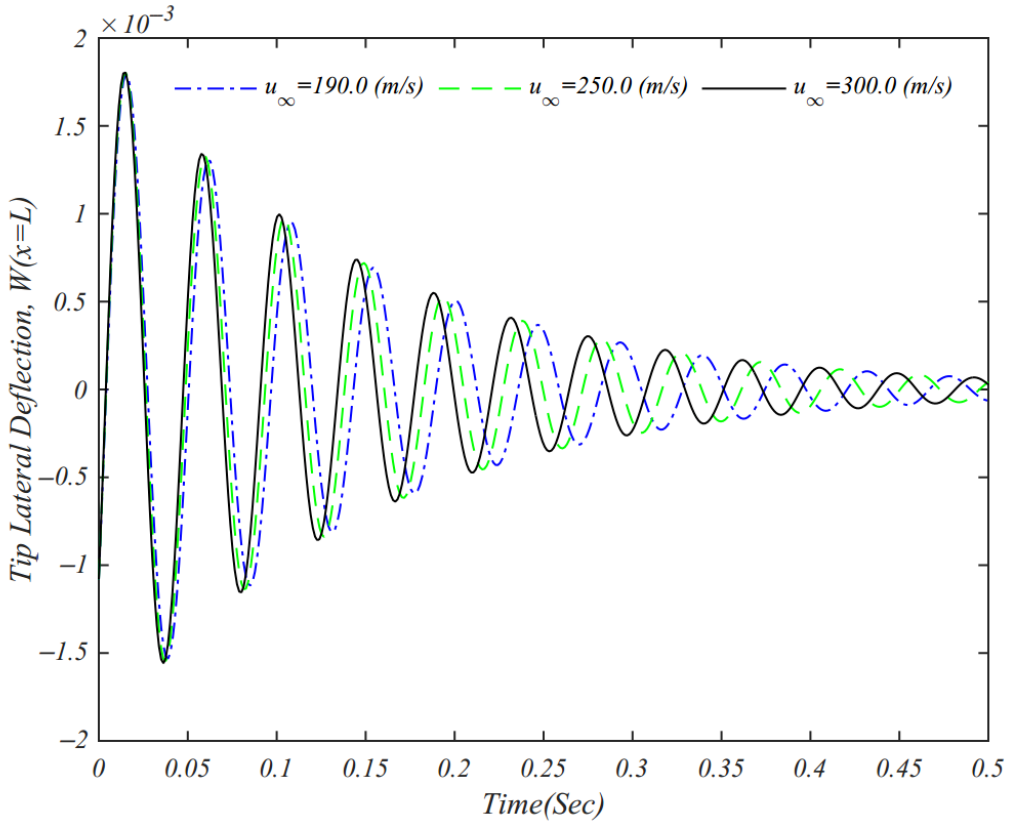

Figure 6. Time history of the system at different free stream air velocities. $M_\infty = 3.0$, $V^*_{CNT} = 017$, $FG - X$.

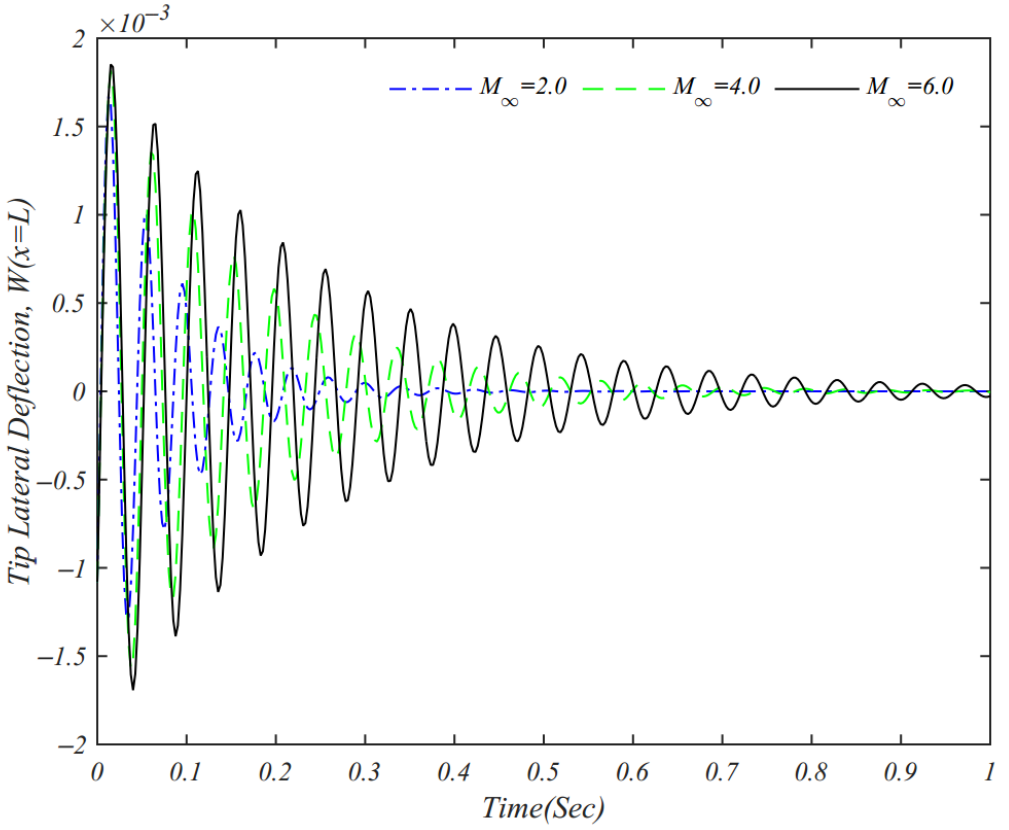

Figure 7. Time history of the system at different Mach numbers. $u_\infty = 230.0\left(\frac{m}{s}\right)$, $V^*_{CNT} = 017$, $FG - X$.

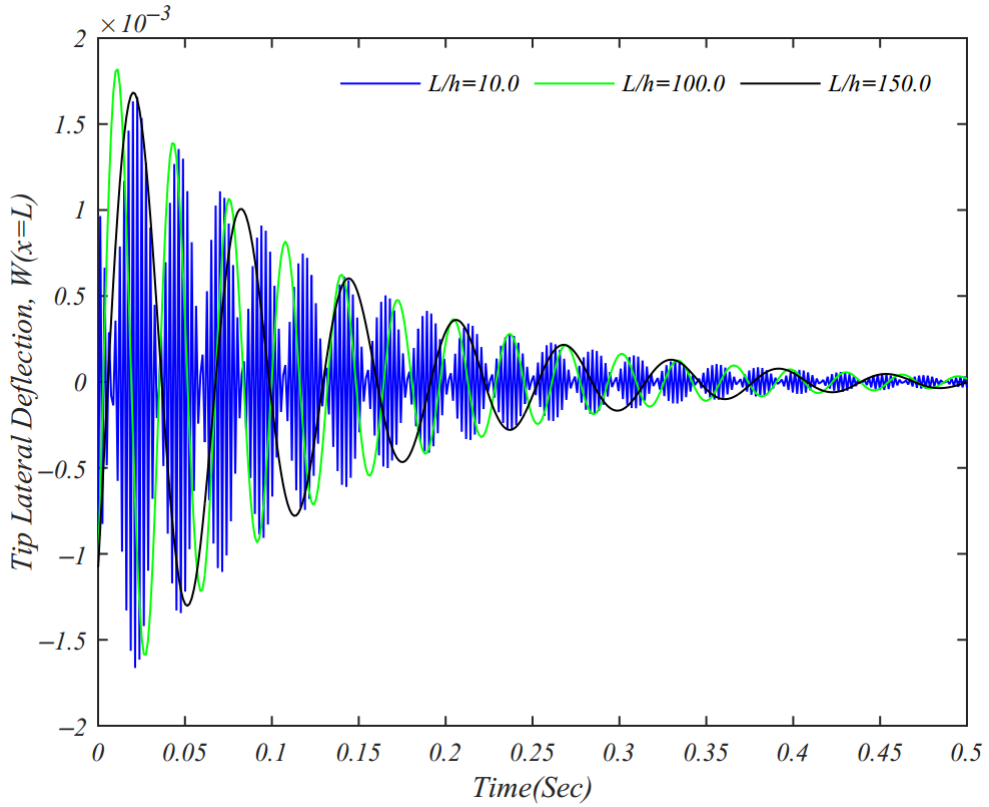

Figure 8. Time history of the system at different slenderness ratios. $u_\infty = 230.0\left(\frac{m}{s}\right)$, $M_\infty = 3.0$, $V^*_{CNT} = 017$, $FG - X$.

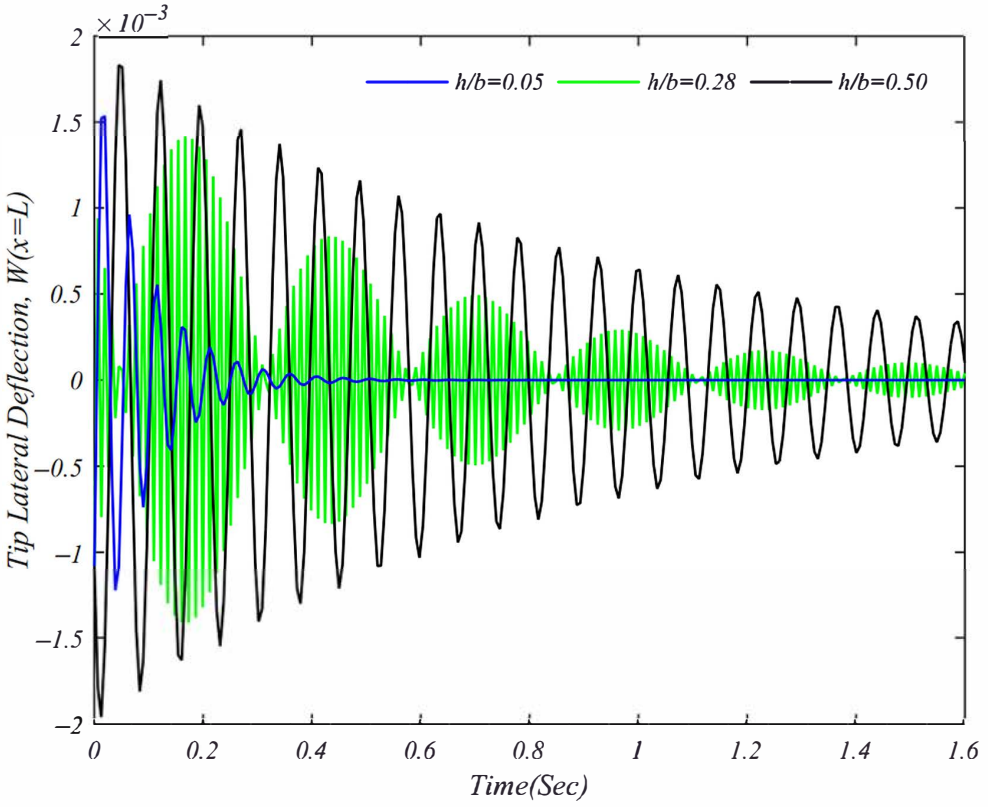

Figure 9. Time history of the system at different thickness ratios. $u_\infty = 230.0\left(\frac{m}{s}\right)$, $M_\infty = 3.0$, $V^*_{CNT} = 017$, $FG - X$.

5. Conclusions

This work focuses on the semi-analytical response of aero-elastic oscillations for cantilever beams reinforced by CNTs, considering four different distributions of the reinforcement phase in the polymeric matrix. A modified third-order piston theory was adopted successfully to model the supersonic air flow rather than a first-order piston theory. The nonlinear dynamic equation was derived from Hamilton's principle, including the Von Kármán nonlinearities. Such an equation was discretized into a nonlinear ordinary differential equation by applying the Galerkin decomposition technique, here solved analytically according to the MTS method. A large systematic investigation has focused on the influence of the reinforcement patterns and volume fraction on the fundamental frequency, free air, and Mach number of the system. From the numerical investigation, the main conclusions can be summarized as follows:

- Composite cantilever beams with *FG-X* reinforcements feature the highest frequency, followed by beams with a uniform reinforcement (*UD-Beam*) and *FG-A* pattern. In all cases, composite structures with an *FG-O* reinforcement pattern show the lowest fundamental frequency.
- The fundamental frequency increases for an increased volume fraction. The effect of the volume fraction on the fundamental frequency is more noticeable at lower slenderness ratios.
- The *CNTR* composite cantilever beam with a *FG-X* reinforcement pattern shows the highest lateral deflection and the highest frequency response, followed by *UD-Beam* and *FG-A* reinforcement pattern. However, the *CNTR* composite cantilever beam with a *FG-O* reinforcement pattern exhibits the lowest lateral dynamical deflection and the lowest frequency response.
- The frequency response increases with the volume fraction of CNTs, due to an overall increased stiffness of the system.
- The frequency response of the system increases by decreasing the slenderness ratio, due to its increased stiffness, up to a certain point, after which we note a reverse behavior with a damped harmonic envelope. This means that the damped beating phenomena occur because the excitation frequency is near the damped natural frequency.
- The frequency response and the lateral dynamic deflection of the system increase for an increased velocity of the free stream air or an increased Mach number. The effect of Mach number is even more pronounced.
- For an increased thickness ratio, the nonlinear frequency response increases significantly. However, the damping rate decreases, which results in an increased lateral deflection.
- Please consider that our findings, especially under varying thickness ratios and high Mach numbers, may be limited by the lack of shear and rotary inertia considerations, as assumed by the Euler–Bernoulli theory. Dynamic modes, indeed, may be influenced by coupled bending and shear effects, especially for short or thick beams subjected to high-speed aerodynamic loading, making the simplifications of Euler–Bernoulli theory more questionable. For these reasons, the Timoshenko theory and higher-order shear deformation theories will be explored in the next work to analyze thick beams and high-speed aeroelastic environments.

Author Contributions: Conceptualization, F.T. and R.D.; Methodology, R.D.; Validation, M.A., F.T. and R.D.; Formal analysis, F.T. and R.D.; Investigation, M.A., F.T. and R.D.; Writing—original draft, M.A.; Writing—review & editing, F.T. and R.D. All authors have read and agreed to the published version of the manuscript.

Funding: This research received no external funding.

Informed Consent Statement: Not applicable.

Data Availability Statement: The original contributions presented in this study are included in the article. Further inquiries can be directed to the corresponding author.

Conflicts of Interest: The authors declare no conflict of interest.

References

1. Cadek, M. Morphological and mechanical properties of carbon-nanotube reinforced semicrystalline and amorphous polymer composites. *Appl. Phys. Lett.* **2002**, *81*, 5123. [CrossRef]
2. Lau, A.K.T.; Hui, D. The revolutionary creation of new advanced materials-carbon nanotube composites. *Compos. Part B* **2002**, *33*, 263–277. [CrossRef]
3. Thostenson, E.T.; Chou, T.W. On the elastic properties of carbon nanotube-based composites: Modelling and characterization. *J. Phys. D Appl. Phys.* **2003**, *36*, 573–582. [CrossRef]
4. Griebel, M.; Hamaekers, J. Molecular dynamic simulations of elastic moduli of polymer-carbon nanotube composites. *Comput. Methods Appl. Mech. Eng.* **2004**, *193*, 1773–1788. [CrossRef]
5. Liew, K.M.; Lei, Z.X.; Zhang, L.W. Mechanical analysis of functionally graded carbon nanotube reinforced composites: A review. *Compos. Struct.* **2015**, *120*, 90–97. [CrossRef]
6. Gojny, F.H.; Wichmann, M.H.G.; Köpke, U.; Fiedler, B.; Schulte, K. Carbon nanotube reinforced epoxy-composites: Enhanced stiffness and fracture toughness at low nanotube content. *Compos. Sci. Technol.* **2004**, *64*, 2363–2371. [CrossRef]
7. Zhou, X.; Shin, E.; Wang, K.W.; Bakis, C.E. Interfacial damping characteristics of carbon nanotube-based composites. *Compos. Sci. Technol.* **2004**, *64*, 2425–2437. [CrossRef]
8. Nayfeh, A.H.; Mook, D.T.; Holmes, P. *Nonlinear Oscillations*; Wiley Publishing: Hoboken, NJ, USA, 1995. [CrossRef]
9. Moon, F.C. *Chaotic and Fractal Dynamics: An Introduction for Applied Scientists and Engineers*; John Wiley & Sons Inc.: New York, NY, USA, 1992.
10. Strogatz, S.H. *Nonlinear Dynamics and Chaos: With Applications to Physics, Biology, Chemistry, and Engineering*; Addison-Wesley Pub.: Reading, MA, USA, 1994.
11. Moon, F.C. Experiments on chaotic motions of a forced nonlinear oscillator: Strange attractors. *J. Appl. Mech.* **1980**, *47*, 638–644. [CrossRef]
12. Tang, D.M.; Dowell, E.H. On the threshold force for chaotic motions for a forced buckled beam. *J. Appl. Mech.* **1988**, *55*, 190–196. [CrossRef]
13. Holmes, P.J.; Moon, F.C. Strange attractors and chaos in nonlinear mechanics. *J. Appl. Mech.* **1983**, *50*, 1021–1032. [CrossRef]
14. Moon, F.C.; Shaw, S.W. Chaotic vibrations of a beam with nonlinear boundary conditions. *Int. J. Non-Linear Mech.* **1983**, *18*, 465–477. [CrossRef]
15. Abhyankar, N.S.; Hall, E.K.; Hanagud, S.V. Chaotic vibrations of beams: Numerical solution of partial differential equations. *J. Appl. Mech.* **1993**, *60*, 167–174. [CrossRef]
16. Hall, E.K.; Hanagud, S.V. Chaos in a single equilibrium point system: Finite deformations. *Nonlin. Dyn.* **1991**, *2*, 157–170. [CrossRef]
17. Tseng, W.Y.; Dugundji, J. Nonlinear vibrations of a buckled beam under harmonic excitation. *J. Appl. Mech.* **1971**, *38*, 467–476. [CrossRef]
18. Hodges, D.H.; Shang, X.; Cesnik, C.E.S. Finite element solution of nonlinear intrinsic equations for curved composite beams. *J. Am. Helicopter Soc.* **1996**, *41*, 313–321. [CrossRef]
19. Virgin, L.N. *Introduction to Experimental Nonlinear Dynamics: A Case Study in Mechanical Vibration*; Cambridge University Press: New York, NY, USA, 2000.
20. Malatkar, P. Nonlinear Vibrations of Cantilever Beams and Plates. Ph.D. Thesis, Virginia Polytechnic Institute and State University, Blacksburg, VA, USA, 2003.
21. Nayfeh, A.H. *Nonlinear Interactions: Analytical, Computational, and Experimental Methods*; John Wiley & Sons Inc.: New York, NY, USA, 2000.
22. Rahman, Z.; Burton, T.D. Large amplitude primary and superharmonic resonances in the Duffing oscillator. *J. Sound Vib.* **1986**, *110*, 363–380. [CrossRef]
23. Hassan, A. On the third superharmonic resonance in the Duffing oscillator. *J. Sound Vib.* **1994**, *172*, 513–526. [CrossRef]
24. Dai, H.H.; Yue, X.K.; Yuan, J.P. A time domain collocation method for obtaining the third superharmonic solutions to the Duffing oscillator. *Nonlinear Dyn.* **2013**, *73*, 593–609. [CrossRef]
25. Song, Z.G.; Li, F.M. Investigations on the flutter properties of supersonic panels with different boundary conditions. *Int. J. Dyn. Control.* **2014**, *3*, 346–353. [CrossRef]

26. Sohn, K.J.; Kim, J.H. Nonlinear thermal flutter of functionally graded panels under a supersonic flow. *Compos. Struct.* **2009**, *88*, 380–387. [CrossRef]
27. Koo, K.N.; Hwang, W.S. Effects of hysteretic and aerodynamic damping on supersonic panel flutter of composite plates. *J. Sound Vib.* **2004**, *273*, 569–583. [CrossRef]
28. Song, Z.G.; Li, F.M. Aeroelastic analysis and active flutter control of nonlinear lattice sandwich beams. *Nonlinear Dyn.* **2014**, *76*, 57–68. [CrossRef]
29. Shin, W.H.; Oh, I.K.; Lee, I. Nonlinear flutter of aerothermally buckled composite shells with damping treatments. *J. Sound Vib.* **2009**, *324*, 556–569. [CrossRef]
30. Natarajan, S.; Kaleeswaran, K.; Manickam, G. Functionally graded material panel flutter by cell-based smoothed finite elements. *J. Coupled Syst. Multiscale Dyn.* **2013**, *1*, 205–215. [CrossRef]
31. Natarajan, S.; Manickam, G.; Bordas, S. Supersonic flutter analysis of functionally graded material plates with cracks. *Front. Aerosp. Eng.* **2013**, *2*, 91–97.
32. Kouchakzadeh, M.A.; Rasekh, M.; Haddadpour, H. Panel flutter analysis of general laminated composite plates. *Compos. Struct.* **2010**, *92*, 2906–2915. [CrossRef]
33. Alimoradzade, M.; Akbas, S.D. Nonlinear thermal vibration of FGM beams resting on nonlinear viscoelastic foundation. *Steel Compos. Struct. Int. J.* **2022**, *44*, 557–567.
34. Camacho, P.; Akhavan, H.; Ribeiro, P. Linear aeroelastic analysis of cantilever hybrid composite laminated plates with curvilinear fibres and carbon nanotubes. *Compos. Struct.* **2021**, *266*, 113765. [CrossRef]
35. Alimoradzadeh, M.; Akbas, S.D. Superharmonic and subharmonic resonances of a carbon nanotube-reinforced composite beam. *Adv. Nano Res.* **2022**, *12*, 353–363.
36. Alimoradzadeh, M.; Tornabene, F.; Esfarjani, S.M.; Dimitri, R. Finite strain-based theory for the superharmonic and subharmonic resonance of beams resting on a nonlinear viscoelastic foundation in thermal conditions, and subjected to a moving mass loading. *Int. J. Non-Linear Mech.* **2023**, *148*, 104271. [CrossRef]
37. Alimoradzadeh, M.; Akbaş, Ş.D. Thermal nonlinear dynamic and stability of carbon nanotube reinforced composite beams. *Steel Compos. Struct.* **2023**, *46*, 637–647.
38. Alimoradzadeh, M.; Heidari, H.; Tornabene, F.; Dimitri, R. Thermo-Mechanical Buckling and Non-Linear Free Oscillation of Functionally Graded Fiber-Reinforced Composite Laminated (FG-FRCL) Beams. *Appl. Sci.* **2023**, *13*, 4904. [CrossRef]
39. Alimoradzadeh, M.; Akbaş, Ş.D. Nonlinear free vibration analysis of a composite beam reinforced by carbon nanotubes. *Steel Compos. Struct.* **2023**, *46*, 335–344.
40. Alimoradzadeh, M.; Akbas, S.D. Nonlinear vibration analysis of carbon nanotube-reinforced composite beams resting on nonlinear viscoelastic foundation. *Geomech. Eng.* **2023**, *32*, 125–135.
41. Kim, N.I.; Jeon, C.K.; Lee, J. Dynamic stability analysis of shear-flexible composite beams. *Arch. Appl. Mech.* **2013**, *83*, 685–707. [CrossRef]
42. Asadi, H.; Beheshti, A.R. On the nonlinear dynamic responses of FG-CNTRC beams exposed to aerothermal loads using third-order piston theory. *Acta Mech.* **2018**, *229*, 2413–2430. [CrossRef]
43. Yao, G.; Zhang, Y.M.; Li, C.Y.; Yang, Z. Stability analysis and vibration characteristics of an axially moving plate in aero-thermal environment. *Acta Mech.* **2016**, *227*, 3517–3527. [CrossRef]
44. Yao, G.; Xie, Z.; Zhu, L.; Zhang, Y. Nonlinear vibrations of an axially moving plate in aero-thermal environment. *Nonlinear Dyn.* **2021**, *105*, 2921–2933. [CrossRef]
45. Alimoradzadeh, M.; Tornabene, F.; Dimitri, R. Nonlinear axial-lateral coupled vibration of functionally graded-fiber reinforced composite laminated (FG-FRCL) beams subjected to aero-thermal loads. *Int. J. Non-Linear Mech.* **2023**, *159*, 104612. [CrossRef]
46. Mohammadimehr, M.; Monajemi, A.A.; Afshari, H. Free and forced vibration analysis of viscoelastic damped FG-CNT reinforced micro composite beams. *Microsyst. Technol.* **2020**, *26*, 3085–3099. [CrossRef]
47. Yas, M.H.; Samadi, N. Free vibrations and buckling analysis of carbon nanotube-reinforced composite Timoshenko beams on elastic foundation. *Int. J. Press. Vessel. Pip.* **2012**, *98*, 119–128. [CrossRef]
48. Fernandes, R.; Mousavi, S.M.; El-Borgi, S. Free and forced vibration nonlinear analysis of a microbeam using finite strain and velocity gradients theory. *Acta Mech.* **2016**, *227*, 2657–2670. [CrossRef]
49. Ramezani, S. A micro scale geometrically non-linear Timoshenko beam model based on strain gradient elasticity theory. *Int. J. Non-Linear Mech.* **2012**, *47*, 863–873. [CrossRef]
50. Shen, H.S. Nonlinear bending of functionally graded carbon nanotube-reinforced composite plates in thermal environments. *Compos. Struct.* **2009**, *91*, 9–19. [CrossRef]
51. McHugh, K.A.; Beran, P.; Freydin, M.; Dowell, E. Flutter and limit cycle oscillations of a cantilevered plate in supersonic/hypersonic flow. In Proceedings of the International Forum on Aeroelasticity and Structural Dynamics (IFASD 2019), Savannah, GA, USA, 10–13 June 2019; Volume 1, pp. 2–3.

52. Samadpour, M.; Asadi, H.; Wang, Q. Nonlinear aero-thermal flutter postponement of supersonic laminated composite beams with shape memory alloys. *Eur. J. Mech. A/Solids* **2016**, *57*, 18–28. [CrossRef]
53. Rao, S.S. *Vibration of Continuous Systems*; Wiley: New York, NY, USA, 23 March 2007.
54. Norouzi, H.; Younesian, D. Chaotic vibrations of beams on nonlinear elastic foundations subjected to reciprocating loads. *Mech. Res. Commun.* **2015**, *69*, 121–128. [CrossRef]
55. Congshuai, H.; Junchao, Z.; Wuchao, C.; Tao, W.; Wei, J.; Dakuan, X.; Hongxing, H. Analysis of three-dimensional thermal vibration coupling characteristics of composite shaft under axial load. *Ocean Eng.* **2023**, *290*, 116341. [CrossRef]